IEEE Open Journal of the
Industrial Electronics Society

Received 1 December 2025; revised 4 February 2026; accepted 9 February 2026. Date of publication 11 February 2026;
date of current version 23 February 2026. The review of this article was arranged by Associate Editor Zhen Zhang.

*Digital Object Identifier 10.1109/OJIES.2026.3663897*

# Hybrid-Timescale Physics-Informed Neural Network for Electrical Equivalent Impedance Identification in Induction Heating Systems

**OSCAR LAHUERTA [1,2] (Graduate Student Member, IEEE), CLAUDIO CARRETERO [2,3] (Senior Member, IEEE), LUIS ANGEL BARRAGAN [1,2], DENIS NAVARRO [1,2], AND JESUS ACERO [1,2] (Senior Member, IEEE)**

[1]Department of Electronic Engineering and Communications, University of Zaragoza, 50018 Zaragoza, Spain
[2]Aragon Institute for Engineering Research (I3A), 50018 Zaragoza, Spain
[3]Department of Applied Physics, University of Zaragoza, 50018 Zaragoza, Spain

CORRESPONDING AUTHOR: OSCAR LAHUERTA (e-mail: olahuerta@unizar.es).

This work was supported in part by project PID2022-136621OBI00, project PDC2023-145837-I00, and project CPP2021-008938, co-funded by MICIU/AEI/10.13039/501100011033, in part by "ERDF A way of making Europe," in part by the "European Union Next Generation EU/PRTR," in part by the DGAFSE under projects PROY T26 24 and PROY T34 24, and in part by the BSH Home Appliances Group.

**ABSTRACT** This article introduces a hybrid variant of a physics-informed neural network (PINN) that is designed to effectively capture both the rapid dynamics of electrical variables and the slower dynamics of state parameters in a domestic induction heating system. By utilizing observable variables, specifically the voltage and current waveforms from the inductor system, the proposed architecture aims to accurately estimate key electrical parameters, i.e., equivalent resistance and inductance, which vary over time due to the nonlinear magnetic properties of the induction load. To assess the performance of the proposed PINN architecture, a comparison with results obtained using an extended Kalman filter was conducted, which serves as a benchmark for this type of task. In addition, the robustness of both approaches was assessed by introducing varying levels of uncertainty in the observable variables. Finally, the effectiveness of both methods was validated through the analysis of experimental measurements collected from a functional prototype.

**INDEX TERMS** Home appliances, induction heating (IH), physics-informed machine learning, system identification.

## I. INTRODUCTION

The introduction of induction heating (IH) technology in the domestic sphere has enabled the development of efficient and safe hobs, [1]. This type of appliance has the basic structure shown in Fig. 1, where the energy supplied by the electrical network is rectified and transformed into a medium-frequency signal that feeds the resonant tank consisting of the inductor-load system, and generally, a series resonance capacitor [2], [3].

The inductor-load system is generally modeled by its electrical equivalent consisting of an *RL*-series circuit, where the resistance, *R*, and inductance, *L*, are related to the power delivered to the load and the stored magnetic energy, respectively, [4], [5]. Both parameters are dependent on various

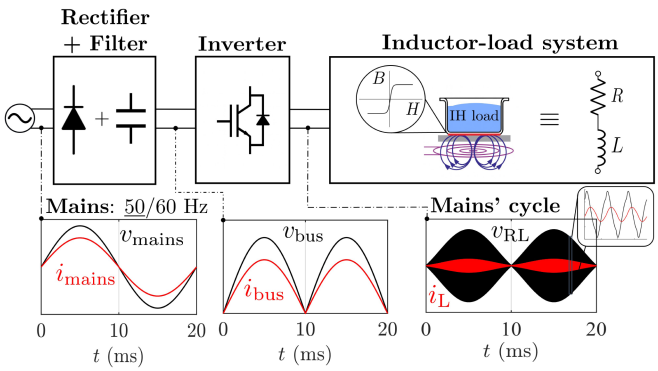


**FIGURE 1.** Schematic DIH system.

operating conditions, and their correct identification from the observable variables given by the voltage, $v_{RL}(t)$, and the current, $i_L(t)$, in the inductor-load system helps improve the user experience in several aspects, such as power control, [6], compliance with EMC regulations, [7], overheating prevention, [8], and automatic pot detection, [9].

Although various analytical models have been proposed to determine the equivalent impedance of the system, [10], [11], these models often rely on highly idealized assumptions, making experimental measurements the preferred method for identification. On one hand, some studies focus on real-time identification using field-programmable gate array implementations [12], [13]. On the other hand, offline large-signal identification is frequently conducted, either through analyzing frequency-domain characteristics [14], [15] or by applying optimization-based approximations [16], [17].

More recently, machine learning techniques [18] and neural networks [19], [20] have been utilized to identify the geometric characteristics of the induction load. However, the application of these techniques for identifying the electrical equivalent of the IH-load has not yet been reported.

Physics-informed neural networks (PINNs) incorporate physical laws by embedding governing differential equations as soft constraints in the loss function, ensuring compliance with physical principles during training, even with sparse or noisy data [21]. They are particularly effective in solving inverse problems, especially in scenarios with nonlinear properties of materials, where analytical solutions are not feasible [22]. As a result, there has been increasing attention to PINNs for system identification across a wide range of domains.

For example, PINN-based methods have been applied to identify thermal parameters in partially known battery physics problems [23] to model the dynamics and estimate parameters from noisy data for autonomous aerial vehicles [24] and to recover heterogeneous profiles estimating velocity and damping parameters in elastic wave problems [25]. The work presented in [26] applies PINNs to identify nonlinear structural systems with a multiphysics damping model, while Gao et al. [27] use them to diagnose faults in complex systems with the physical knowledge about the interdependences among sensors and Chen et al. [28] developed an online torque prediction for electric motor control.

PINNs have also shown excellent performance in more classic physics domains. In fluid mechanics, they can be used to reconstruct hidden flow fields by encoding the Navier–Stokes equations into the network [29]. Similarly, the work presented in [30] embedded fluid dynamic principles into a neural network for traffic flow prediction. In power systems, researchers have applied PINNs to model and identify grid dynamics, for instance, Misyris et al. [31] used them to enforce power balance equations in predicting system transients, and Zhao et al. [32] achieved accurate parameter estimation in power electronic converters by incorporating the converter's differential equations into the learning process. Moreover, recent applications span biomedicine for blood-flow and ultrasound-driven parameter estimation [33], [34], robotics for joint-level dynamics identification [35], electromagnetics and microwaves for inverse design of devices [36], [37], acoustics [38], and even quantum control [39].

These successes in the different areas highlight the growing consensus that PINNs can serve as a tool for system identification and dynamic modeling, providing physically consistent and data-efficient learning even for complex, multiphysics problems. Building on these advances, this article employs a PINN to identify equivalent resistance and inductance parameters, moving beyond traditional black-box modeling, [40]. The performance of the proposed PINN architecture is evaluated against an extended Kalman filter (EKF), [41], which has been successfully employed in related applications [42], [43].

The main contributions of this work are as follows.

1) It proposes a hybrid-timescale PINN architecture for electrical equivalent impedance identification, estimating resistance and inductance parameters directly from observable voltage and current waveforms.
2) The IH system identification is addressed using a dual-branch frequency partitioned scheme that explicitly separates fast switching dynamics from the slow envelope-driven parameter drift using disjoint Fourier feature embeddings.
3) It provides a comprehensive assessment against the EKF baseline, including simulation-based validation and experimental verification on a laboratory prototype, thereby outperforming this method and other existing approaches reported in the literature.

The rest of this article is organized as follows. Section II begins with a further description of the problem and proposes the architecture of the hybrid PINN. Then, in Section III, the EKF is described. Next, in Section IV, the electromagnetic simulation model used as reference is presented. Section V presents the core results, comparing the state variable estimates by each method. Section VI is dedicated to experimental verification. Finally, Section VII concludes this article.

## II. PHYSICS-INFORMED NEURAL NETWORK

### A. PROBLEM DESCRIPTION

The observable variables, $v_{RL}(t)$ and $i_L(t)$, are periodic with a fundamental at the switching frequency $f_{sw}$. The proposed identification method relies on these voltage and current measurements that are connected through the system's electrical state equation, assuming that the domestic induction heating (DIH) system can be represented by a resistance and inductance series

$$v_{RL}(t) = R(t) \cdot i_L(t) + L(t) \cdot \frac{di_L(t)}{dt}. \tag{1}$$

In the DIH system under study, Fig. 1, due to the low filter's capacitance, the inverter input voltage follows the rectified mains' waveform, so the inductor current amplitude is modulated at mains' frequency, $f_{mains} = 50/60$ Hz, with period

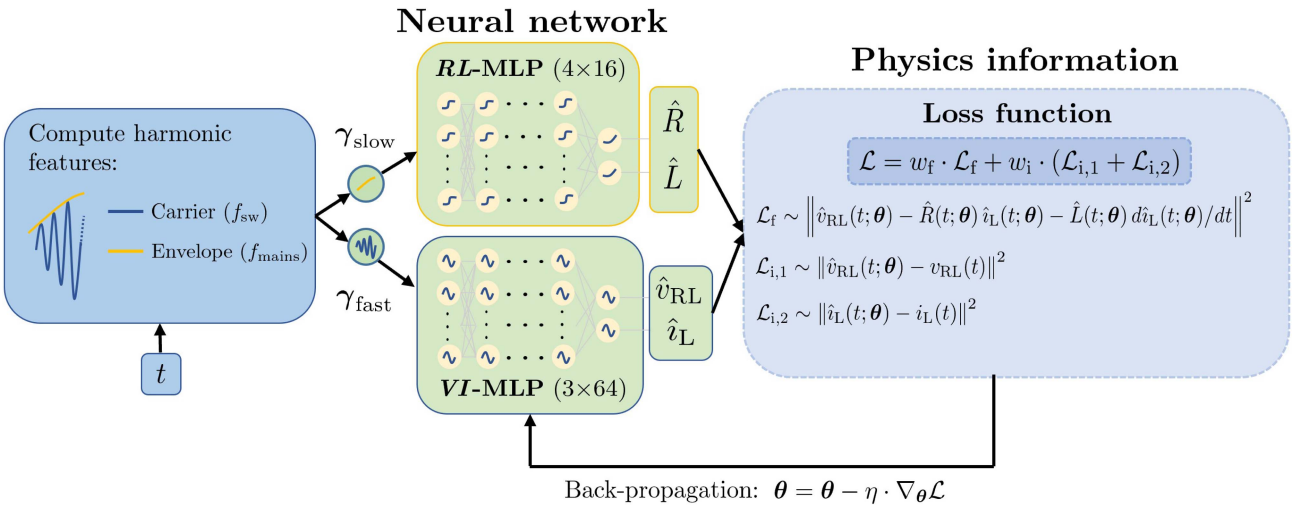


**FIGURE 2.** Schematic representation of the PINN.

$T_B = (2f_{mains})^{-1}$. This yields two natural time scales: a slow dynamic associated with the envelope evolution at $f_{mains}$ and a fast dynamic corresponding to the carrier wave whose frequency is determined by the switching frequency, $f_{sw}$.

Thus, the problem reduces to identifying a resistance and inductance, the complexity of which lies in the fact that these parameters depend, among others, on frequency and the excitation level because the IH load material exhibits nonlinear magnetization [44]. The magnetic flux density, $B$, in the vessel, is the response of the magnetic material to the magnetic field strength, $H$, generated by the inductor: $B = \mu_0 \mu_{r,load}(H)H$, where $\mu_{r,load}(H)$ is the relative magnetic permeability of the material and depends on $H$, which, in turn depends on the load current, $i_L(t)$. As the rectified mains modulates the current amplitude [15], the operating point along the $B - H$ curve drifts, so the equivalent resistance, $R(t)$, and inductance, $L(t)$, vary in time. In this work, since resistance and inductance are assumed to depend on the current amplitude, which is modulated by the mains' envelope, they follow the slow dynamics. Conversely, voltage and current evolve according to the fast dynamic.

### B. HYBRID-TIMESCALE ARCHITECTURE

A well-documented limitation of standard PINNs is spectral bias, which is the tendency to fit low frequencies first and struggle with high-frequency content [45]. To address this in the DIH system, where signals combine a high-frequency switching carrier with a low-frequency envelope, a two-timescale PINN that explicitly separates fast waveform dynamics from slow parameter dynamics is adopted as Fig. 2 shows. Prior work has explored scale-separated PINNs to mitigate spectral bias [46], but their application to electrical equivalent impedance estimation in DIH has not been reported.

The gradient-based training dynamics of PINNs can be approximated by a linearized regime governed by the neural tangent kernel (NTK), [47]. Under this approximation, the training residual error decomposes into NTK eigenmodes, each decaying at a rate proportional to its associated eigenvalue. This yields a principled interpretation of spectral bias: high-frequency components tend to align with NTK modes associated with smaller eigenvalues and are, therefore, learned more slowly than low-frequency content [48]. Moreover, Fourier feature mappings mitigate this effect by reshaping the effective kernel spectrum [49], increasing the model's ability to represent and learn high-frequency functions. In this work, we take a further step by partitioning the Fourier features by construction, which induces two specialized hypothesis spaces with reduced cross-scale coupling and ensures that each branch's training dynamics (kernel) is concentrated on the appropriate spectral content. This limits high-frequency leakage into the parameter-estimation branch and improves optimization stability and convergence in hybrid-timescale identification.

In the context of the article, the identification problem can be formulated as an inverse problem, where $\boldsymbol{\lambda}(t) = (R(t), L(t))$ denotes the parameters to obtain. The inputs to the PINN are the time instants, $t \in \Omega = [0, T_B]$ and the outputs are the estimated voltage and current and the parameters to identify: $\hat{v}_{RL}(t;\boldsymbol{\theta})$, $\hat{i}_L(t;\boldsymbol{\theta})$, and $\hat{\boldsymbol{\lambda}}(t;\boldsymbol{\theta})$ with $\boldsymbol{\theta}$ being the neural network's weights and biases.

The time $t$ is embedded into a Fourier mapping $\boldsymbol{\gamma}(t)$, [48], consisting of cosine–sine pairs at selected base frequencies and their harmonics, which then feed disjoint subsets to each branch so that each multilayer perceptron (MLP) specializes in its time scale.

On one hand, the *VI*-MLP captures the fast dynamics associated with the switching frequency, estimating voltage and current. The $m$th component of the Fourier mapping is

$$\boldsymbol{\gamma}^m_{fast}(t) = [\sin(2\pi(2m+1)f_{sw}t), \cos(2\pi(2m+1)f_{sw}t)]. \tag{2}$$

where $m = 1, \ldots, N_{\text{sw}}$ is the harmonic number of the switching frequency and $\boldsymbol{\gamma}_{\text{fast}}(t) = [\boldsymbol{\gamma}^1_{\text{fast}}(t), \ldots, \boldsymbol{\gamma}^{N_{\text{sw}}}_{\text{fast}}(t)]$. The network comprises three hidden layers with 64 neurons each and uses the $\sin(\cdot)$ activation function, leveraging the periodicity of the signals.

On the other hand, the *RL*-MLP captures the slow envelope dynamics and outputs the estimation of resistance and inductance. The $n$th component of the Fourier mapping is

$$\boldsymbol{\gamma}^n_{\text{slow}}(t) = [\sin(2\pi(2n+1)(2f_{\text{mains}})t), \cos(2\pi(2n+1)(2f_{\text{mains}})t)] \tag{3}$$

where $n = 1, \ldots, N_{\text{mains}}$ is the harmonic number of the mains' frequency and $\boldsymbol{\gamma}_{\text{slow}}(t) = [\boldsymbol{\gamma}^1_{\text{slow}}(t), \ldots, \boldsymbol{\gamma}^{N_{\text{mains}}}_{\text{slow}}(t)]$. It is a four-layer neural network with 16 neurons per layer with $\tanh(\cdot)$ as the activation function and the neurons in the output layer are $\text{softplus}(\cdot) = \ln(1 + e^{(\cdot)})$ to ensure the positivity of the outputs.

Values of $N_{\text{sw}} = 3$ and $N_{\text{mains}} = 1$ are tuned manually. These values should only be increased if the loss reduces substantially as they increase the computational cost.

The residuals of the loss function are constructed as follows:

$$\mathcal{L}_{\text{f}} = \frac{1}{|T_{\text{f}}|} \sum_{t \in T_{\text{f}}} \left|\left| \hat{v}_{\text{RL}}(t;\boldsymbol{\theta}) - \hat{R}(t;\boldsymbol{\theta}) \cdot \hat{i}_{\text{L}}(t;\boldsymbol{\theta}) - \hat{L}(t;\boldsymbol{\theta}) \cdot \frac{d\hat{i}_{\text{L}}(t;\boldsymbol{\theta})}{dt} \right|\right|^2_2 \tag{4}$$

$$\mathcal{L}_{\text{i},1} = \frac{1}{|T_{\text{i}}|} \sum_{t \in T_{\text{i}}} \left|\left| \hat{v}_{\text{RL}}(t;\boldsymbol{\theta}) - v_{\text{RL}}(t) \right|\right|^2_2 \tag{5}$$

and

$$\mathcal{L}_{\text{i},2} = \frac{1}{|T_{\text{i}}|} \sum_{t \in T_{\text{i}}} \left|\left| \hat{i}_{\text{L}}(t;\boldsymbol{\theta}) - i_{\text{L}}(t) \right|\right|^2_2. \tag{6}$$

For simplicity, the training domains were chosen to be identical $T_{\text{f}} = T_{\text{i}} = \Omega = [0, T_{\text{B}}]$ and consist of $|T_{\text{f}}| = |T_{\text{i}}| = T_{\text{B}} \cdot f_{\text{s}}$ evenly distributed time collocation points where $f_{\text{s}} = 50$ Ms/s is the sampling frequency. To facilitate training and convergence [50], the neural network is provided with normalized reference voltage and current; this normalization is achieved by dividing each signal by its maximum value during the mains' cycle.

Training is performed end-to-end by minimizing $\mathcal{L}$ via back-propagation

$$\mathcal{L} = w_{\text{f}} \cdot \mathcal{L}_{\text{f}} + w_{\text{i}} \cdot (\mathcal{L}_{\text{i},1} + \mathcal{L}_{\text{i},2}) \tag{7}$$

where $w_{\text{f}} = 5$ and $w_{\text{i}} = 1$ are chosen to balance the contributions of the physical and waveform residuals. The gradient of the total loss propagates through the harmonic feature mapping and both MLPs: the physics term sends gradients to the *RL*-MLP through $\hat{R}(t;\boldsymbol{\theta})$ and $\hat{L}(t;\boldsymbol{\theta})$, while the data terms guide the *VI*-MLP through $\hat{v}_{\text{RL}}(t;\boldsymbol{\theta})$ and $\hat{i}_{\text{L}}(t;\boldsymbol{\theta})$. This coupling drives the *VI*-MLP to match the measured waveforms at the switching frequency while remaining consistent with the nonlinear governing equation, and it regularizes the *RL*-MLP toward physically plausible parameter values.

To evaluate the term $\mathcal{L}_{\text{f}}$, the time derivative $d\hat{i}_{\text{L}}(t;\boldsymbol{\theta})/dt$ was obtained by automatic differentiation (AD) using the PyTorch library from Python. AD [51] is a differentiation technique that applies the chain rule to a computational graph of elementary operations. Unlike finite-difference schemes, AD yields gradients that are exact up to machine precision without step-size tuning. In this setting, $\hat{i}_{\text{L}}(t)$ is a successive composition of differentiable functions: the Fourier feature embedding and the *VI*-MLP, so its derivative is obtained by propagating the chain rule through both the embedding and the network.

## III. EXTENDED KALMAN FILTER

The Kalman filter (KF) is a recursive algorithm designed to estimate the states of a dynamic system from noisy measurements. Consider a linear system represented in discrete time by the following equations, which govern its dynamics:

$$\mathbf{x}_{\text{k}+1} = \mathbf{F}_{\text{k}} \cdot \mathbf{x}_{\text{k}} + \mathbf{G}_{\text{k}} \cdot \mathbf{u}_{\text{k}} + \mathbf{w}_{\text{k}} \tag{8}$$

$$y_{\text{k}} = \mathbf{C}_{\text{k}} \cdot \mathbf{x}_{\text{k}} + \mathbf{D}_{\text{k}} \cdot \mathbf{u}_{\text{k}} + v_{\text{k}} \tag{9}$$

where $\mathbf{x}_{\text{k}}$ is the state vector at instant $k$, $\mathbf{u}_{\text{k}}$ represents the input vector, $y_{\text{k}}$ the output quantity, $\mathbf{w}_{\text{k}}$ is the process noise vector, and $v_{\text{k}}$ represents the measurement noise and have associated noise matrices $\boldsymbol{\Sigma}_{\text{w}}$ and variance $\Sigma_{\text{v}}$, respectively.

The discrete-time state equation used in the KF is

$$v_{\text{RL,k}} = \theta_{1,\text{k}} \cdot i_{\text{L,k}} + \theta_{2,\text{k}} \cdot \left(\frac{di_{\text{L}}}{dt}\right)_{\text{k}} \tag{10}$$

where $(di_{\text{L}}/dt)_{\text{k}}$ is a numerical approximation of the current derivative at instant $k$; $\theta_{2,\text{k}} = L_{\text{k}}/T_{\text{s}}$ is chosen to achieve normalization by keeping its magnitude comparable to $\theta_{1,\text{k}} = R_{\text{k}}$ and $T_{\text{s}} = 1/f_{\text{s}}$ is the sampling period of $v_{\text{RL}}(t)$ and $i_{\text{L}}(t)$.

To estimate the resistance $R_{\text{k}}$ and inductance $L_{\text{k}}$, it is assumed that the parameters $\theta_{\text{k}} = (\theta_{1,\text{k}}, \theta_{2,\text{k}})$ vary slowly, and the system can be described as follows:

$$\theta_{\text{k}+1} = \theta_{\text{k}} + \mathbf{w}_{\text{k}} \tag{11}$$

$$y_{\text{k}} = \mathbf{z}^T_{\text{k}} \cdot \theta_{\text{k}} + v_{\text{k}}. \tag{12}$$

Comparing the system described by (8) and (9), with the one described by (11) and (12), it follows that $\mathbf{x}_{\text{k}} = \boldsymbol{\theta}_{\text{k}}$, $\mathbf{F}_{\text{k}} = \mathbb{I}$, $\mathbf{G}_{\text{k}} = \mathbf{0}$, $\mathbf{C}_{\text{k}} = \mathbf{z}^T_{\text{k}}$, and $\mathbf{D}_{\text{k}} = \mathbf{0}$. Finally, by comparing (10) and (12), it can be inferred that

$$\mathbf{z}^T_{\text{k}} = [i_{\text{L,k}}, (di_{\text{L}}/dt)_{\text{k}}] \tag{13}$$

$$y_{\text{k}} = v_{\text{RL,k}}. \tag{14}$$

Although it is straightforward to implement, this KF formulation exhibits poor performance in this DIH application, especially in the resistance estimation. The reason is the high sensitivity to the discrete-time derivative as numerical differentiation amplifies noise and any prefiltering of $i_{\text{L}}(t)$ introduces bias and phase lag. As a result, the following KF variant is used in order to improve the performance.

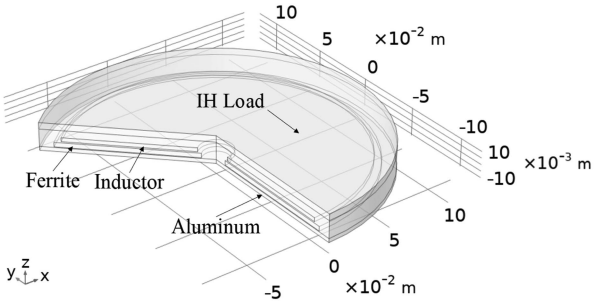


**FIGURE 3.** Electromagnetic simulation model in COMSOL.

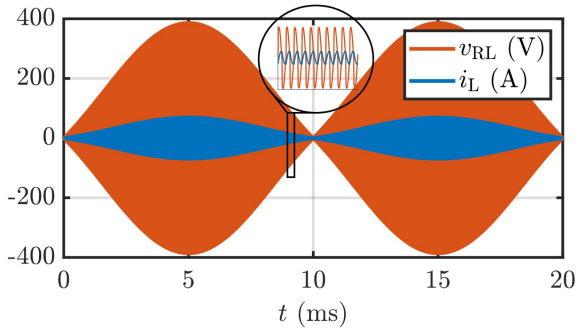


**FIGURE 4.** Voltage and current waveforms obtained through time-domain simulation in COMSOL within mains' cycle $2{\cdot}T_B$ (20 ms).

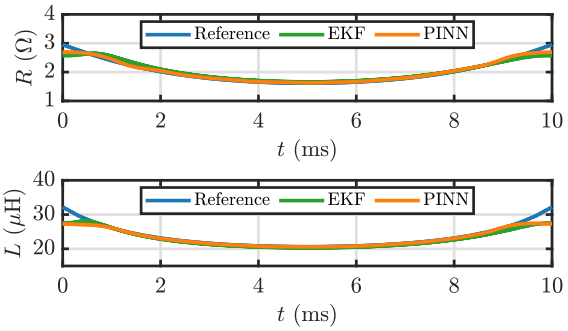


**FIGURE 5.** Comparison between the resistance and inductance values obtained from the identification algorithms and the results obtained from COMSOL for $f_{sw}$ = 45 kHz.

The EKF is applied to nonlinear systems described by the following equations:

$$\mathbf{x}_{k+1} = \mathbf{f}(\mathbf{x}_k, \mathbf{u}_k) + \mathbf{w}_k \tag{15}$$

$$\mathbf{y}_k = \mathbf{h}(\mathbf{x}_k, \mathbf{u}_k) + \mathbf{v}_k \tag{16}$$

where $\mathbf{f}(\mathbf{x}_k, \mathbf{u}_k)$ is a nonlinear state-transition function and $\mathbf{h}(\mathbf{x}_k, \mathbf{u}_k)$ is a nonlinear measurement function.

In the KF description before, the current derivative is known, obtained via external derivative filters. However, this work seeks to verify performance and assess results when that assumption is not met. In other words, when the current derivative is treated as an additional state variable that the EKF itself must estimate. Now the system is nonlinear and $\mathbf{x}_k = (x_{1,k}, x_{2,k}, x_{3,k}, x_{4,k})$, where $x_{1,k} = i_{L,k}$, $x_{2,k} = (di_L/dt)_k$, $x_{3,k} = R_k$, and $x_{4,k} = L_k/T_s$. Therefore

$$\mathbf{f}(\mathbf{x}_k, \mathbf{u}_k) = [x_{1,k} + x_{2,k} \cdot T_s, x_{2,k}, x_{3,k}, x_{4,k}]^T \tag{17}$$

$$\mathbf{h}(\mathbf{x}_k, \mathbf{u}_k) = [x_{1,k}, x_{1,k} \cdot x_{3,k} + x_{2,k} \cdot x_{4,k}]^T. \tag{18}$$

Once the two identification algorithms have been described, the electromagnetic simulation that will enable a preliminary validation of the results of both methods is presented in the following section.

## IV. SIMULATION MODEL

The structure of the DIH system is based on an axisymmetric model using COMSOL multiphysics[1] (COMSOL) for the electromagnetic simulation and is illustrated in Fig. 3. This DIH model comprises the following components. The IH load is a magnetic and electrical conductor with Frohlich nonlinear magnetic relationship, $\mu_{r,load}(H) = \alpha/(b\mu_0(\alpha + H)^2)$ with $\alpha$ = 1500 A/m and $b = 0.5$ T$^{-1}$ [52], which models the change in cookware material magnetic permeability with the level of excitation during the mains' cycle, and an electrical conductivity $\sigma_{load} = 8{\cdot}10^6$ S/m.

At a distance of $d_{load\text{-}coil} = 5.5$ mm below, the inductor is placed. Made of copper, it is composed of $n_t = 23$ turns evenly distributed between the internal radius $r_{int} = 12.5$ mm and the external radius $r_{ext} = 105$ mm. It is modeled by an impressed constant current density assuming the homogenization of the turns into the cross-sectional area of the coil, $\mathbf{J}_{coil} = n_t i_{L,0}/S_{coil}\hat{\varphi}$, directed along the azimuthal axis, where $i_{L,0}$ is the current amplitude and $S_{coil} = t_{coil} \cdot (r_{ext} - r_{int})$ with thickness $t_{coil} = 3$ mm. This component is placed at a distance $d_{coil\text{-}f} = 1$ mm above the flux concentrator plate, which is made of high-permeability ferrite. The ferrite is intended to concentrate the electromagnetic field flux inside the IH system and it is located at a distance $d_{f\text{-}al} = 0.5$ mm above the aluminum plane, which is placed for shielding purposes.

Two types of simulations are employed in this work. Time-domain simulations are computationally expensive and are used to extract voltage and current waveforms, $v_{RL}(t)$ and $i_L(t)$. Fig. 4 illustrates the waveforms generated from this time-domain simulation. The DIH system is excited with a square voltage waveform of variable amplitude $230\sqrt{2}|\sin(2\pi f_{mains} \cdot t)|$ V, which emulates the voltage modulation, and frequency $f_{sw}$, with rise and fall time $t_r = t_f = 0.2$ $\mu$s. Finally, a resonant capacitor $C_r = 1080$ nF is placed at the output.

The other type of simulation that can be performed is frequency-domain simulation. In these simulations, $R$ and $L$ are obtained as frequency-dependent functions that account for other properties of the materials. Specifically, they can be readily determined from the complex-valued induced coil

[1]Registered trademark.

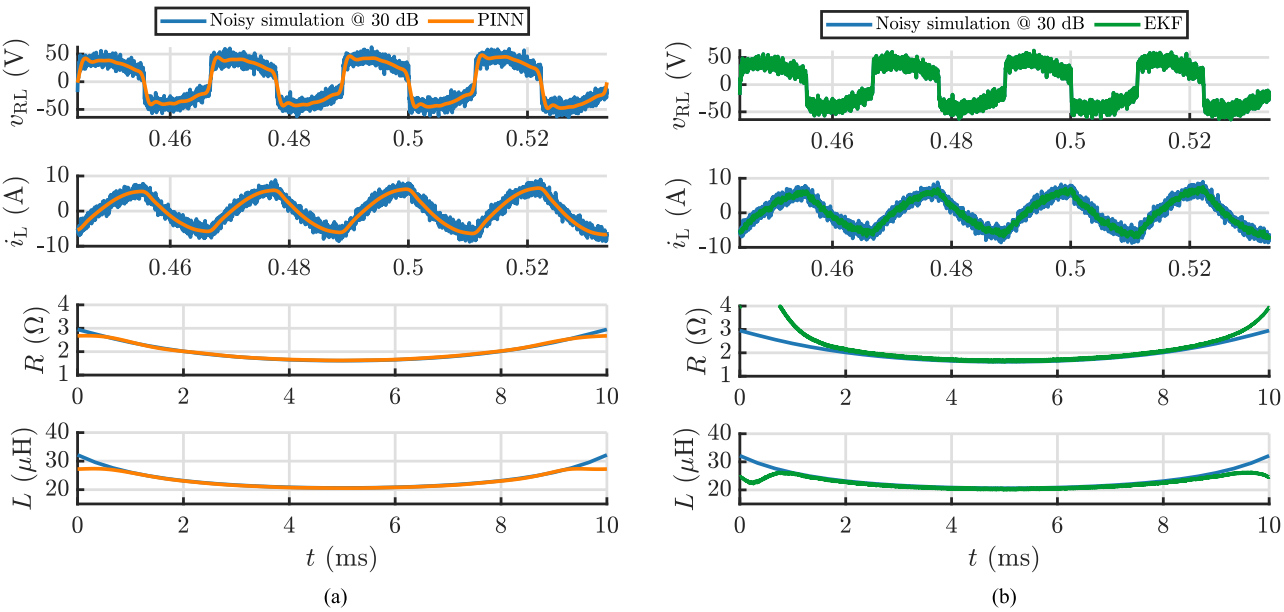


**FIGURE 6.** Comparison between the EKF and PINN methods and simulation results for noisy conditions for $f_{sw} = 45$ kHz. (a) PINN identification. (b) EKF identification.

voltage, $v_{coil}$, computed by integrating the azimuthal component of the electric field along the coil turns. Then, $v_{coil}/i_{L,0} = R + j2\pi f_{sw}L$. The results obtained in this simulation will be used to validate the effectiveness of the identification algorithms in the following section.

## V. METHOD COMPARISON

Fig. 5 shows the comparison between the results in the identification for the tested methods and the results extracted from frequency-domain simulation. PINN uses Xavier–Glorot initialization, [53], and Adam optimizer with constant learning rate, $\eta = 10^{-3}$. The EKF is initialized with $\hat{x}_0^+ = \mathbf{0}$ and $\mathbf{\Sigma}_{x,0}^+ = 10^3 \cdot \mathbb{I}$. Its noise matrices are

$$\mathbf{\Sigma}_w^{EKF} = \begin{pmatrix} 10^{-1} & 0 & 0 & 0 \\ 0 & 10^{-1}/T_s & 0 & 0 \\ 0 & 0 & 10^{-7} & 10^{-5} \\ 0 & 0 & 10^{-5} & 10^{-6} \end{pmatrix}, \quad \Sigma_v^{EKF} = 1. \tag{19}$$

In practice, only the ratio $\mathbf{\Sigma}_w/\Sigma_v$ matters for the EKF gain scaling, therefore, $\Sigma_v^{EKF} = 1$ is fixed and $\mathbf{\Sigma}_w^{EKF}$ is tuned manually, assigning higher process noise to fast-changing states and lower to slow ones.

For identification, the data efficiency of PINNs is leveraged. PINNs can be trained with scarce datasets because the physics residual constrains the hypothesis space, enabling accurate inference from few data [21]. Accordingly, the PINN is trained on just a mains' half-cycle (10 ms) and a downsampling $D_s = 10$ is applied, which reduces the number of collocation points, and thus, the training cost. With this setting, the PINN was trained for 5000 epochs using graphics processing unit (GPU) acceleration with compute unified device architecture (CUDA), requiring 31.3 s on an NVIDIA RTX PRO 4000 (Blackwell, 24-GB GDDR7). By contrast, the EKF estimation is ran over a mains' cycle (20 ms) to tradeoff noise rejection and latency in $R$ and $L$ tracking, and since it exhibits an initial transient before converging, only the last 10 ms are shown. The EKF implemented in MATLAB required 13.2 s for the same dataset.

To quantitatively compare the parameter estimates produced by the two methods, the mean relative error (MRE) is proposed as a figure of merit, $\text{MRE}_X\ (\%) = 100/N_s \sum_{k=1}^{N_s} |\hat{X}_k - X_k|/X_k$, where $\hat{X}_k$ and $X_k$ represent the resistance ($R_k$) or the inductance ($L_k$) in the iteration $k$ estimated by the algorithms and those extracted from the frequency-domain simulation, respectively, and $N_s$ is the number of samples from the electromagnetic simulation.

In addition, the normalized mean squared error (NMSE) has been chosen as the figure of merit for the observable variables, voltage, and current. The estimated signals, $\hat{s}_k$, by each method were compared against noise-free experimental signals, $s_k$, filtered using a Butterworth low-pass filter with a cutoff frequency $f_c = 0.5$ MHz. Mathematically, $\text{NMSE}_s\ (\%) = 100 \sum_{k=1}^{N_s} (\hat{s}_k - s_k)^2 / \sum_{k=1}^{N_s} s_k^2$.

The MRE in resistance ($\text{MRE}_R$) and in inductance ($\text{MRE}_L$) at various switching frequencies is reported in Table 1. The results show strong agreement with frequency-domain simulations across the full frequency range: the PINN attains constant errors of 1.6% in resistance and 2.0% in inductance. In contrast, the EKF exhibits markedly higher errors at all switching frequencies, which vary as frequency rises, worsening from 3.1% to 5.5% in resistance and from 2.4% to 2.8% in inductance.

**TABLE 1. Comparison of Errors for Noiseless Signals**

| $f_{sw}$ (kHz) | Error | PINN | EKF |
|---|---|---|---|
| 45 | $MRE_R$ (%) | 1.68 | 3.11 |
| | $MRE_L$ (%) | 1.81 | 2.42 |
| 50 | $MRE_R$ (%) | 1.12 | 4.04 |
| | $MRE_L$ (%) | 1.71 | 2.68 |
| 60 | $MRE_R$ (%) | 1.66 | 4.62 |
| | $MRE_L$ (%) | 2.14 | 2.81 |
| 70 | $MRE_R$ (%) | 1.68 | 5.54 |
| | $MRE_L$ (%) | 2.03 | 2.82 |

**TABLE 2. Comparison of Errors for Noisy Signals**

(a) Error in resistance, $MRE_R$ (%).

| $f_{sw}$ (kHz) | SNR (dB) | | | | | |
|---|---|---|---|---|---|---|
| | 70 | | 50 | | 30 | |
| | PINN | EKF | PINN | EKF | PINN | EKF |
| 45 | 2.30 | 2.87 | 1.63 | 2.85 | 1.46 | 11.24 |
| 50 | 2.37 | 4.02 | 1.58 | 4.01 | 2.70 | 8.98 |
| 60 | 1.53 | 4.54 | 2.39 | 4.54 | 2.26 | 6.05 |
| 70 | 1.98 | 5.62 | 1.54 | 5.62 | 2.20 | 6.31 |

(b) Error in inductance, $MRE_L$ (%).

| $f_{sw}$ (kHz) | SNR (dB) | | | | | |
|---|---|---|---|---|---|---|
| | 70 | | 50 | | 30 | |
| | PINN | EKF | PINN | EKF | PINN | EKF |
| 45 | 2.57 | 2.68 | 1.90 | 2.70 | 1.89 | 4.28 |
| 50 | 2.39 | 3.06 | 1.92 | 3.08 | 2.03 | 3.42 |
| 60 | 2.01 | 3.39 | 1.99 | 3.40 | 1.82 | 4.16 |
| 70 | 2.19 | 3.49 | 1.98 | 3.49 | 1.83 | 4.12 |

**TABLE 3. Comparison of Errors for Noisy Signals**

(a) Error in voltage, $NMSE_v$ (%).

| $f_{sw}$ (kHz) | SNR (dB) | | | | | |
|---|---|---|---|---|---|---|
| | 70 | | 50 | | 30 | |
| | PINN | EKF | PINN | EKF | PINN | EKF |
| 45 | 0.17 | 0.44 | 0.18 | 0.44 | 0.19 | 0.54 |
| 50 | 0.27 | 0.64 | 0.26 | 0.64 | 0.26 | 0.74 |
| 60 | 0.44 | 1.06 | 0.40 | 1.06 | 0.42 | 1.16 |
| 70 | 0.66 | 1.48 | 0.62 | 1.48 | 0.58 | 1.58 |

(b) Error in current, $NMSE_i$ (%).

| $f_{sw}$ (kHz) | SNR (dB) | | | | | |
|---|---|---|---|---|---|---|
| | 70 | | 50 | | 30 | |
| | PINN | EKF | PINN | EKF | PINN | EKF |
| 45 | 0.03 | 0.00 | 0.02 | 0.01 | 0.02 | 0.02 |
| 50 | 0.03 | 0.01 | 0.03 | 0.01 | 0.04 | 0.02 |
| 60 | 0.04 | 0.01 | 0.05 | 0.01 | 0.05 | 0.03 |
| 70 | 0.06 | 0.02 | 0.05 | 0.02 | 0.05 | 0.04 |

**TABLE 4. Comparison of Errors in Waveforms for the Tested Methods**

| $f_{sw}$ (kHz) | Noise std $\sigma$ (SNR) | Error | PINN | EKF |
|---|---|---|---|---|
| 45 | 3.55 V (34 dB) | $NMSE_v$ (%) | 0.46 | 0.49 |
| | 0.07 A (50 dB) | $NMSE_i$ (%) | 0.18 | 0.46 |
| 50 | 3.29 V (33 dB) | $NMSE_v$ (%) | 0.55 | 0.62 |
| | 0.07 A (48 dB) | $NMSE_i$ (%) | 0.26 | 0.65 |
| 60 | 2.77 V (34 dB) | $NMSE_v$ (%) | 0.65 | 0.68 |
| | 0.07 A (45 dB) | $NMSE_i$ (%) | 0.39 | 0.95 |
| 70 | 2.45 V (35 dB) | $NMSE_v$ (%) | 0.67 | 0.69 |
| | 0.07 A (44 dB) | $NMSE_i$ (%) | 0.46 | 1.19 |

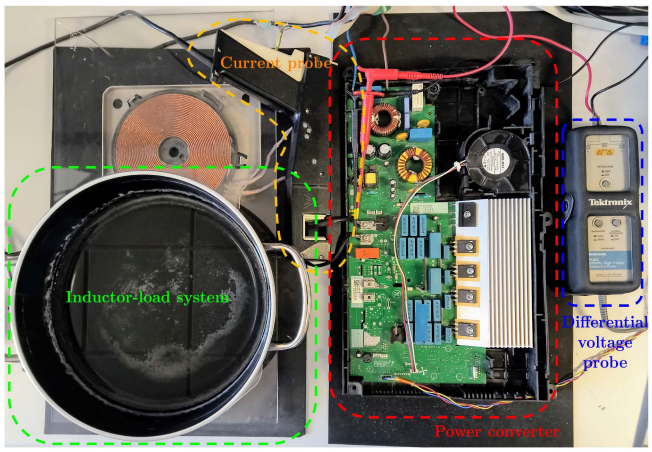


**FIGURE 7. Experimental setup.**

From the maximum and minimum values of the reference inductance, it can be determined that the system's resonance frequency lies in the interval $f_{res} \in [27, 36]$ kHz. When the switching frequency departs from this resonance, errors grow because extra harmonics appear, which is the drawback of the identification algorithms based on frequency-domain and optimization methods reported in literature [17], and it also affects the EKF. Nevertheless, the PINN remains robust, as its *VI*-MLP branch captures both the fundamental and harmonic features.

Most of the error stems from the end instants, $t \approx 0$ and $t \approx T_B$, of the identification interval, where both algorithms underestimate the parameters, as can be seen in Fig. 5. However, this is not a significant issue because at those time points the delivered power is low due to the low amplitude of the signals, and it is more important for the identification to be accurate at intermediate instants within this interval.

Regarding the errors in $\hat{v}_{RL}$ and $\hat{\imath}_L$, PINN and EKF reproduce the waveforms correctly, obtaining $NMSE_v \sim 0.01\%$ and $0.00\%$ , and $NMSE_i \sim 0.02\%$ and $0.00\%$ , respectively. The PINN shows estimation errors that arise mainly at the rising and falling switching edges of the voltage, where a slight

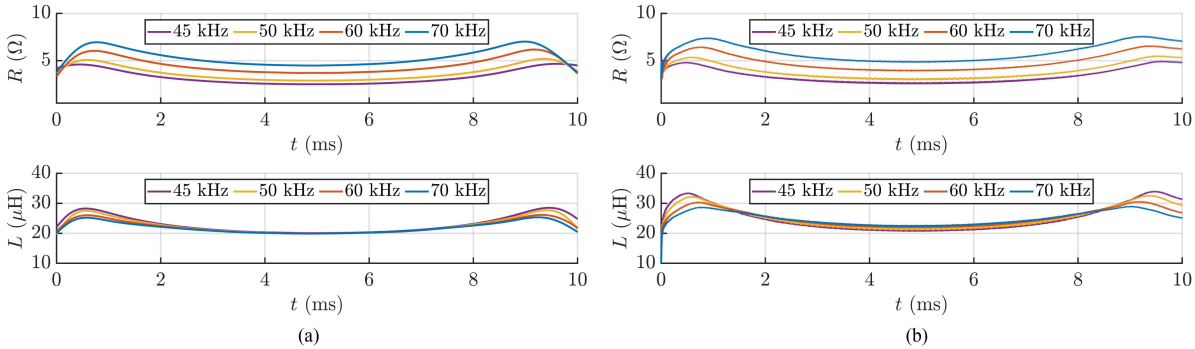


**FIGURE 8.** Experimental identification results. (a) PINN identification. (b) EKF identification.

ringing occurs, whereas the EKF reproduces both signals perfectly. The key difference is that the EKF reconstructs the signals at each instant and computes values of the parameters to ensure a correct fit. The PINN, by contrast, uses the entire time window of the identification interval and fits every time collocation point simultaneously in each training epoch.

### A. PERFORMANCE UNDER NOISE

This section will evaluate the identification results by incorporating noise into the reference voltage and current signals. To this end, white Gaussian noise, $\varepsilon(t) \sim \mathcal{N}(0, \sigma^2)$, was added to these waveforms with $\sigma^2 = P_{\text{signal}}/10^{\text{SNR(dB)}/10}$ where $P_{\text{signal}} = 1/N_{\text{s}} \sum_{\text{k}=1}^{N_{\text{s}}} s_{\text{k}}^2$. The input waveforms provided to the methods will be $\tilde{s}(t) = s(t) + \varepsilon(t)$.

Fig. 6 compares the algorithms' results against the COMSOL references. PINN [see Fig. 6(a)] matches the waveforms except for short, localized discrepancies at the sharp switching edges of $\hat{v}_{\text{RL}}$, where high-frequency content causes brief ringing. EKF [see Fig. 6(b)] closely tracks the noise ripples in the measured signals but this causes the estimates of $\hat{R}$ and $\hat{L}$ to absorb measurement fluctuations, which degrades parameter accuracy. Because the PINN enforces the governing differential equation, random noise cannot satisfy the physics, and thus, does not bias the calculated parameters; the network acts simultaneously as estimator and filter. This behavior is reflected during training as the data term $\mathcal{L}_{\text{i}} = \mathcal{L}_{\text{i},1} + \mathcal{L}_{\text{i},2}$ saturates at the noise floor, while the physics term $\mathcal{L}_{\text{f}}$ keeps decreasing, indicating that the model refines $\hat{R}$, $\hat{L}$, $\hat{v}_{\text{RL}}$, and $\hat{i}_{\text{L}}$ to satisfy the differential constraint without overfitting.

Quantitatively, as presented in Tables 2 and 3, the PINN attains consistently lower $\text{MRE}_{\text{R}}$ and $\text{MRE}_{\text{L}}$ than the EKF with the gap widening as signal-to-noise ratio (SNR) decreases. For waveform errors, the PINN also yields lower voltage NMSE in all cases, whereas the EKF reports slightly smaller current NMSE because it follows the noise. This pattern follows from the NMSE evaluation: errors are computed against noiseless reference waveforms. Consequently, although the EKF reconstructs the noisy signal point by point, it incurs larger errors relative to the clean references, whereas the PINN effectively filters out noise. Overall, the PINN produces smooth, physically plausible trajectories and more accurate parameter estimates, and its advantage becomes more pronounced in noisier conditions and also at higher $f_{\text{sw}}$ due to increased harmonic content.

## VI. EXPERIMENTAL RESULTS

The identification results presented in Section V used data extracted from the electromagnetic simulation as a first step toward the identification task. Nevertheless, to demonstrate the feasibility of the proposed identification techniques for the real DIH system, several measurements have been conducted. The experimental setup (see Fig. 7) consists of a planar spiral inductor with an external diameter of 21 cm placed over a ferrite disk. The IH load is a ferromagnetic pot of stainless steel with a base diameter of 18 cm.

This inductor-load system is connected to a power converter, which is controlled by an open-loop software. Four steady-state operating points were selected by varying $f_{\text{sw}}$ to 45, 50, 60, and 70 kHz. At each operating point, voltage and current measurements have been captured by means of a Tektronix DPO7354 oscilloscope, using a TCP303 current probe and a P5205 differential voltage probe, respectively.

The experimental identification results are shown in Table 4. In addition, for each $f_{\text{sw}}$, some experimental noise level estimations have been calculated. The value of $\sigma$ is computed as the variance of the difference between the noisy experimental signal and the filtered experimental signal.

Because no experimental reference values for resistance and inductance are available, validation focuses on how well the reconstructed waveforms reproduce the measurements at each operating point. Results show that the PINN has better overall performance than the EKF. Although the experimental noise levels in voltage ($\sim$ 35 dB, dominated by switching ringing from parasitic inductances) and current ($\sim$ 45 dB, primarily device-originated) are not excessively high, they are sufficient to degrade the EKF identification, whose estimates are affected by the propagation of that noise from the observable variables to the estimated parameters. Moreover, tuning the process noise matrices is challenging: conservative choices that stabilize the filter introduce phase delay, aggressive choices reduce delay at the expense of noisier parameter

traces. By contrast, the two-scale PINN (fast branch for the carrier and harmonics; slow branch for parameter regularization) embeds the governing physics and naturally rejects random fluctuations, avoiding switching-frequency oscillations in the reconstructions. This is reflected in the parameters estimated by the methods; see Fig. 8.

Using the maximum and minimum inductance values estimated by the PINN, the experimental resonance frequency can be determined to lie within $f_{\text{res}} \in [29, 34]$ kHz. The evolution of the waveform error with switching frequency also follows the expected trend, worsening the identification as it moves away from resonance. This degradation is notable for the EKF in current ($\text{NMSE}_\text{i}$ from 0.46% to 1.19% ), whereas it is less pronounced for the PINN ($\text{NMSE}_\text{i}$ from 0.18% to 0.46% ) with the decrease in SNR also being a factor to consider. However, for both algorithms the $\text{NMSE}_\text{v}$ remains practically constant across the entire frequency range, which suggests that harmonic distortion is primarily suffered by the current.

The PINN produces cleaner and more physically consistent parameter trajectories; see Fig. 8(a). Over each mains half-cycle, the estimated $\hat{R}$ and $\hat{L}$ are nearly symmetric about the midpoint: at $t = 0$ and $t = T_\text{B}$, the curves are essentially mirror images and reach comparable values. In contrast, the EKF traces become visibly asymmetric near the edges, with unequal peaks and small time shifts, consistent with the filter's phase lag and the variance accumulated in the state update; see Fig. 8(b).

## VII. CONCLUSION

This article presents a hybrid-timescale PINN that identifies the equivalent parameters of a DIH system directly from voltage and current waveforms capturing both fast switching-carrier dynamics and the slow parameter drift driven by the IH load nonlinear magnetization. Its dual-branch architecture, combined with a Fourier input mapping, avoids spectral bias and causes each branch to specialize at its timescale.

Across simulations and experiments, the PINN consistently reconstructed electrical waveforms and produced parameter estimates with small, frequency-independent errors. It was notably more accurate and noise-robust than the EKF variant and previously published methods, making it a strong candidate for precise parameter identification in DIH appliances.

## REFERENCES


[1] J. Acero et al., "Domestic induction appliances," *IEEE Ind. Appl. Mag.*, vol. 16, no. 2, pp. 39–47, Mar./Apr. 2010.

[2] O. Lucia, P. Maussion, E. J. Dede, and J. M. Burdio, "Induction heating technology and its applications: Past developments, current technology, and future challenges," *IEEE Trans. Ind. Electron.*, vol. 61, no. 5, pp. 2509–2520, May 2014.

[3] C. Carretero, O. Lucia, J. Acero, R. Alonso, and J. Burdio, "Frequency-dependent modelling of domestic induction heating systems using numerical methods for accurate time-domain simulation," *IET Power Electron.*, vol. 5, pp. 1291–1297, 2012.

[4] F. Forest, E. Laboure, F. Costa, and J. Gaspard, "Principle of a multi-load/ single converter system for low power induction heating," *IEEE Trans. Power Electron.*, vol. 15, no. 2, pp. 223–230, Mar. 2000.

[5] P. Guillen, H. Sarnago, J. Acero, J. M. Burdio, S. Llorente, and O. Lucia, "Induction heating appliances: Fifty years of technological success: Paving the path for sustainable homes," *IEEE Ind. Electron. Mag.*, vol. 19, no. 3, pp. 51–66, Sep. 2025.

[6] D. Paesa, S. Llorente, C. Sagues, and O. Aldana, "Adaptive observers applied to pan temperature control of induction hobs," *IEEE Trans. Ind. Appl.*, vol. 45, no. 3, pp. 1116–1125, May/Jun. 2009.

[7] J. Villa, A. Dominguez, L. A. Barragan, J. I. Artigas, J. Espanol, and D. Navarro, "Conductance control for electromagnetic-compatible induction heating appliances," *IEEE Trans. Power Electron.*, vol. 37, no. 3, pp. 2909–2920, Mar. 2022.

[8] C. Franco, J. Acero, R. Alonso, C. Sagues, and D. Paesa, "Inductive sensor for temperature measurement in induction heating applications," *IEEE Sensors J.*, vol. 12, no. 5, pp. 996–1003, May 2012.

[9] A. Bono, B. M. del Brio, C. Bernal, F. J. Perez, A. Martinez, and I. Sanz, "The inductor as a smart sensor for material identification in domestic induction cooking," *IEEE Sensors J.*, vol. 18, no. 6, pp. 2462–2470, Mar. 2018.

[10] J. Acero, R. Alonso, J. Burdio, L. A. Barragan, and D. Puyal, "Analytical equivalent impedance for a planar circular induction heating system," *IEEE Trans. Magn.*, vol. 42, no. 1, pp. 84–86, Jan. 2006.

[11] C. Carretero, J. Acero, R. Alonso, J. M. Burdio, and F. Monterde, "Embedded ring-type inductors modeling with application to induction heating systems," *IEEE Trans. Magn.*, vol. 45, no. 12, pp. 5333–5343, Dec. 2009.

[12] O. Jimenez, O. Lucia, I. Urriza, L. A. Barragan, and D. Navarro, "Analysis and implementation of FPGA-based online parametric identification algorithms for resonant power converters," *IEEE Trans. Ind. Inform.*, vol. 10, no. 2, pp. 1144–1153, May 2014.

[13] D. Navarro, O. Lucia, L. A. Barragan, I. Urriza, and O. Jimenez, "High-level synthesis for accelerating the FPGA implementation of computationally demanding control algorithms for power converters," *IEEE Trans. Ind. Inform.*, vol. 9, no. 3, pp. 1371–1379, Aug. 2013.

[14] D. Puyal, C. Bernal, J. M. Burdio, J. Acero, and I. Millan, "Versatile high-frequency inverter module for large-signal inductive loads characterization up to 1.5 MHz and 7 kW," *IEEE Trans. Power Electron.*, vol. 23, no. 1, pp. 75–87, Jan. 2008.

[15] J. Villa, L. A. Barragan, J. I. Artigas, D. Navarro, A. Dominguez, and T. Cabeza, "SoC-based in-cycle load identification of induction heating appliances," *IEEE Trans. Ind. Electron.*, vol. 68, no. 8, pp. 6762–6772, Aug. 2021.

[16] A. Dominguez, A. Otin, I. Urriza, L. A. Barragan, D. Navarro, and J. Artigas, "Load identification of domestic induction heating based on particle swarm optimization," in *Proc. Workshop Control Model. Power Electron.*, 2014, pp. 1–6.

[17] O. Lahuerta, C. Carretero, L. A. Barragan, and J. Acero, "Comparative analysis of identification methods for estimating the electrical equivalent circuit of domestic induction heating systems," in *Proc. IEEE Int. Conf. Ind. Technol.*, 2024, pp. 1–6.

[18] J. Villa, D. Navarro, A. Dominguez, J. I. Artigas, and L. A. Barragan, "Vessel recognition in induction heating appliances—A deep-learning approach," *IEEE Access*, vol. 9, pp. 16053–16061, 2021.

[19] O. Lucia, D. Navarro, P. Guillen, H. Sarnago, and S. Lucia, "Deep learning-based magnetic coupling detection for advanced induction heating appliances," *IEEE Access*, vol. 7, pp. 181668–181677, 2019.

[20] A. Bono, C. Bernal, B. M. del Brio, F. J. Perez, and A. Martinez, "Applications of machine learning in induction cooking," in *Proc. Annu. Conf. IEEE Ind. Electron. Soc.*, 2016, pp. 849–854.

[21] M. Raissi, P. Perdikaris, and G. Karniadakis, "Physics-informed neural networks: A deep learning framework for solving forward and inverse problems involving nonlinear partial differential equations," *J. Comput. Phys.*, vol. 378, pp. 686–707, 2019.

[22] S. Falas, M. Asprou, C. Konstantinou, and M. K. Michael, "Robust power system state estimation using physics-informed neural networks," *IEEE Trans. Ind. Inform.*, vol. 21, no. 10, pp. 8057–8067, Oct. 2025.

[23] Y. B. He, B. C. Wang, H. P. Deng, and H. X. Li, "Physics-reserved spatiotemporal modeling of battery thermal process: Temperature prediction, parameter identification, and heat generation rate estimation," *J. Energy Storage*, vol. 75, 2024, Art. no. 109604.

[24] D. Bianchi, N. Epicoco, M. Di Ferdinando, S. Di Gennaro, and P. Pepe, "Physics-informed neural networks for unmanned aerial vehicle system estimation," *Drones*, vol. 8, no. 12, 2024, Art. no. 716.

[25] A. Pakravan, "One-dimensional elastic and viscoelastic full-waveform inversion in heterogeneous media using physics-informed neural networks," *IEEE Access*, vol. 12, pp. 69922–69940, 2024.
[26] T. Liu and H. Meidani, "Physics-informed neural networks for system identification of structural systems with a multiphysics damping model," *J. Eng. Mechan.*, vol. 149, no. 10, 2023, Art. no. 04023079.
[27] Y. Gao, Z. Zhong, M. Ma, Z. Zhang, Y. Zhang, and C. Wang, "Physics-embedded recurrent graph neural network for fault diagnosis of complex systems," *IEEE Access*, vol. 12, pp. 122426–122436, 2024.
[28] Y. Chen, Y. Xiao, C. Ji, and B. Su, "An online torque prediction method of PMSM using PINNs," *IEEE Access*, vol. 13, pp. 196796–196808, 2025.
[29] M. Raissi, A. Yazdani, and G. E. Karniadakis, "Hidden fluid mechanics: Learning velocity and pressure fields from flow visualizations," *Science*, vol. 367, no. 6481, pp. 1026–1030, 2020.
[30] D. Li, J. Zhang, Y. Liu, J. Zhang, H. Xi, and Q. Yang, "Embedding fluid dynamics into neural networks: Toward interpretable traffic flow prediction via physics-informed learning," *IEEE Internet Things J.*, vol. 12, no. 16, pp. 34528–34547, Aug. 2025.
[31] G. S. Misyris, A. Venzke, and S. Chatzivasileiadis, "Physics-informed neural networks for power systems," in *Proc. IEEE Power Energy Soc. Gen. Meeting*, 2020, pp. 1–5.
[32] S. Zhao, Y. Peng, Y. Zhang, and H. Wang, "Parameter estimation of power electronic converters with physics-informed machine learning," *IEEE Trans. Power Electron.*, vol. 37, no. 10, pp. 11567–11578, Oct. 2022.
[33] J. Garay, J. Dunstan, S. Uribe, and F. S. Costabal, "Physics-informed neural networks for parameter estimation in blood flow models," *Comput. Biol. Med.*, vol. 178, 2024, Art. no. 108706.
[34] H. J. Ling et al., "Physics-guided neural networks for intraventricular vector flow mapping," *IEEE Trans. Ultrason., Ferroelectr., Freq. Control*, vol. 71, no. 11, pp. 1377–1388, Nov. 2024.
[35] Z. Li, S. Wu, W. Chen, and F. Sun, "Physics-informed neural networks for compliant robotic manipulators dynamic modeling," *J. Comput. Sci.*, vol. 90, 2025, Art. no. 102633.
[36] M. Baldan, P. Di Barba, and D. A. Lowther, "Physics-informed neural networks for inverse electromagnetic problems," *IEEE Trans. Magn.*, vol. 59, no. 5, May 2023, Art. no. 7001705.
[37] Y. Q. Pan, R. Wang, and B. Z. Wang, "Physics-informed neural networks with embedded analytical models: Inverse design of multilayer dielectric-loaded rectangular waveguide devices," *IEEE Trans. Microw. Theory Tech.*, vol. 72, no. 7, pp. 3993–4005, Jul. 2024.
[38] C. Song, T. Alkhalifah, and U. B. Waheed, "Solving the frequency-domain acoustic VTI wave equation using physics-informed neural networks," *Geophys. J. Int.*, vol. 225, no. 2, pp. 846–859, 2021.
[39] A. Norambuena, M. Mattheakis, F. J. Gonzalez, and R. Coto, "Physics-informed neural networks for quantum control," *Phys. Rev. Lett.*, vol. 132, no. 1, 2024, Art. no. 010801.
[40] G. Karniadakis, Y. Kevrekidis, L. Lu, P. Perdikaris, S. Wang, and L. Yang, "Physics-informed machine learning," *Nat. Rev. Phys.*, vol. 3, pp. 422–440, 2021.
[41] R. Yildiz, M. Barut, and E. Zerdali, "A comprehensive comparison of extended and unscented Kalman filters for speed-sensorless control applications of induction motors," *IEEE Trans. Ind. Inform.*, vol. 16, no. 10, pp. 6423–6432, Oct. 2020.
[42] F. Auger, M. Hilairet, J. M. Guerrero, E. Monmasson, T. Orlowska-Kowalska, and S. Katsura, "Industrial applications of the Kalman filter: A review," *IEEE Trans. Ind. Electron.*, vol. 60, no. 12, pp. 5458–5471, Dec. 2013.
[43] O. Lahuerta, C. Carretero, L. A. Barragan, and J. Acero, "Comparative study of Kalman filters for electrical identification in domestic induction systems," in *Proc. Annu. Conf. IEEE Ind. Electron. Soc.*, 2025, pp. 1–6.
[44] J. Serrano, J. Acero, I. Lope, C. Carretero, J. M. Burdio, and R. Alonso, "Modeling of domestic induction heating systems with non-linear saturable loads," in *Proc. IEEE Appl. Power Electron. Conf. Expo.*, 2017, pp. 3127–3133.
[45] B. C. Wang, Z. D. Ji, Y. Wang, H. X. Li, and Z. Li, "A physics-informed composite network for modeling of electrochemical process of large-scale lithium-ion batteries," *IEEE Trans. Ind. Inform.*, vol. 21, no. 1, pp. 287–296, Jan. 2025.
[46] D. A. Serino, A. Alvarez, J. Burby, I. G. Kevrekidis, and Q. Tang, "Fast-slow neural networks for learning singularly perturbed dynamical systems," *J. Comput. Phys.*, vol. 537, 2025, Art. no. 114090.
[47] S. Wang, X. Yu, and P. Perdikaris, "When and why PINNs fail to train: A neural tangent kernel perspective," *J. Comput. Phys.*, vol. 449, 2022, Art. no. 110768.
[48] S. Wang, H. Wang, and P. Perdikaris, "On the eigenvector bias of fourier feature networks: From regression to solving multi-scale PDEs with physics-informed neural networks," *Comput. Methods Appl. Mech. Eng.*, vol. 384, 2021, Art. no. 113938.
[49] M. Tancik et al., "Fourier features let networks learn high frequency functions in low dimensional domains," in *Proc. Adv. Neural Inf. Process. Syst.*, 2020, pp. 7537–7547.
[50] W. Qiu, Q. Tang, J. Liu, and W. Yao, "An automatic identification framework for complex power quality disturbances based on multifusion convolutional neural network," *IEEE Trans. Ind. Inform.*, vol. 16, no. 5, pp. 3233–3241, May 2020.
[51] T. Wang, R. Skulstad, and H. Zhang, "Physics-informed neural networks for robust system identification of ship roll dynamics with noise resilience," *IEEE Trans. Ind. Inform.*, vol. 21, no. 5, pp. 3934–3942, May 2025.
[52] O. Lahuerta, J. Ortega, C. Carretero, J. P. Martinez, and J. Acero, "Frohlich model characterization of magnetic properties of the induction heating load," *COMPEL—Int. J. Comput. Math. Electr. Electron. Eng.*, vol. 43, no. 6, pp. 1127–1138, 2024.
[53] H. Wang, S. Ma, L. Dong, S. Huang, D. Zhang, and F. Wei, "DeepNet: Scaling transformers to 1,000 layers," *IEEE Trans. Pattern Anal. Mach. Intell.*, vol. 46, no. 10, pp. 6761–6774, Oct. 2024.

**OSCAR LAHUERTA** (Graduate Student Member, IEEE) received the M.Sc. degree in physics in 2024 from the University of Zaragoza, Zaragoza, Spain, where he is currently working toward the Ph.D. degree in electronic engineering.

His research interests include nonlinear modeling and application of artificial intelligence techniques in induction heating systems.

Mr. Lahuerta is a member of the Aragon Institute for Engineering Research (I3A), Group of Power Electronics and Microelectronics (GEPM).

**CLAUDIO CARRETERO** (Senior Member, IEEE) received the M.Sc. degree in physics and the M.Eng. and Ph.D. degrees in electrical engineering from the University of Zaragoza, Zaragoza, Spain, in 1998, 2002, and 2010, respectively.

He is an Associate Professor with the Department of Applied Physics, University of Zaragoza. His research interests include induction heating applications and electromagnetic modeling of inductive systems.

Dr. Carretero is a Member of the Aragon Institute for Engineering Research (I3A), Group of Power Electronics and Microelectronics (GEPM).

**LUIS ANGEL BARRAGAN** received the M.Sc. and Ph.D. degrees in physics from the University of Zaragoza, Zaragoza, Spain, in 1988 and 1993, respectively.

He is a Professor with the Department of Electronic Engineering and Communications, University of Zaragoza. He has been involved in different research and development projects on induction-heating systems for home appliances. His research interests include modeling and digital control applied to domestic induction heating.

Dr. Barragan is a Member of the Aragon Institute for Engineering Research (I3A), Group of Power Electronics and Microelectronics (GEPM).

**DENIS NAVARRO** received the M.Sc. degree in microelectronics from the University of Montpellier, Montpellier, France, in 1987, and the Ph.D. degree in microelectronics from the University of Zaragoza, Zaragoza, Spain, in 1992 .

Since 1988, he has been with the Department of Electronic Engineering and Communications, Universidad de Zaragoza, where he is currently a Professor. In 1993, he designed the first SPARC microprocessor in Europe. He is involved in the implementation of new applications of integrated circuits. His current research interests include computer-aided design for very-large-scale integration, low-power application-specific integrated circuit design, and modulation techniques for power converters.

Dr. Navarro is a Member of the Aragon Institute for Engineering Research (I3A), Group of Power Electronics and Microelectronics (GEPM).

**JESUS ACERO** (Senior Member, IEEE) received the M.Sc. and Ph.D. degrees in electrical engineering from the University of Zaragoza, Zaragoza, Spain, in 1992 and 2005, respectively.

He is a Professor with the Department of Electronic Engineering and Communications, University of Zaragoza. His research interests include resonant converters for induction heating applications, inductive-type load modeling, and magnetics.

Dr. Acero has been an Associate Editor for IEEE TRANSACTIONS ON POWER ELECTRONICS since 2015. He is a Member of the Aragon Institute for Engineering Research (I3A), Group of Power Electronics and Microelectronics (GEPM).